A Low-Profile Autonomous Interface Circuit for Piezoelectric Micro-Power Generators

Berkay Çiftci, *Graduate Student Member, IEEE*, Salar Chamanian, *Member, IEEE*, Aziz Koyuncuoğlu, Ali Muhtaroğlu, *Senior Member, IEEE*, and Haluk Külah, *Member, IEEE*

***Abstract*— This paper presents a low-profile and autonomous piezoelectric energy harvesting system consisting of an extraction rectifier and a maximum power point tracking (MPPT) circuit for powering portable electronics. Synchronized switch harvesting on capacitor-inductor (SSHCI) technique with its unique two-step voltage flipping process is utilized to downsize the ponderous external inductor and extend application areas of such harvesting systems. SSHCI implementation with small flipping inductor-capacitor combination enhances voltage flipping efficiency and accordingly attains power extraction improvements over conventional synchronized switch harvesting on inductor (SSHI) circuits utilizing bulky external components. A novel MPPT system provides robustness of operation against changing load and excitation conditions. Innovation in MPPT comes from the refresh unit, which continually monitors excitation conditions of piezoelectric harvester to detect any change in optimum storage voltage. Compared with conventional circuits, optimal flipping detection inspired from active diode structures eliminates the need for external adjustment, delivering autonomy to SSHCI. Inductor sharing between SSHCI and MPPT reduces the number of external components. The circuit is fabricated in 180 nm CMOS technology with 1.23 mm^2 active area, and is tested with custom MEMS piezoelectric harvester at its resonance frequency of 415 Hz. It is capable of extracting 5.44x more power compared to ideal FBR, while using 100μ H inductor. Due to reduction of losses through low power design techniques, measured power conversion efficiency of 83% is achieved at 3.2 V piezoelectric open circuit voltage amplitude. Boosting of power generation capacity in a low profile is a significant contribution of the design.**

***Index Terms*— Autonomous, low-profile, piezoelectric energy harvester, self-adapting, SSHCI, MPPT, IC.**

Manuscript received September 8, 2020; revised December 7, 2020 and January 4, 2021; accepted January 15, 2021. Date of publication February 1, 2021; date of current version March 8, 2021. This work was supported by the European Research Council (ERC) through the European Union's Horizon 2020 Research and Innovation Programme under Grant 682756. This article was recommended by Associate Editor A. Worapishet. *(Corresponding author: Berkay Çiftci.)*

Berkay Çiftci and Salar Chamanian are with the Department of Electrical and Electronics Engineering, Middle East Technical University (METU), 06800 Ankara, Turkey (e-mail: cberkay@metu.edu.tr; salar.chamanian@metu.edu.tr).

Aziz Koyuncuoğlu is with the METU-MEMS Research and Application Center, 06800 Ankara, Turkey (e-mail: akoyuncuoglu@mems.metu.edu.tr).

Ali Muhtaroğlu is with the Department of Electrical and Electronics Engineering, Middle East Technical University Northern Cyprus Campus (METU-NCC), 99738 Güzelyurt, Turkey, and also with the Center for Sustainability, Middle East Technical University Northern Cyprus Campus (METU-NCC), 99738 Güzelyurt, Turkey (e-mail: amuhtar@metu.edu.tr).

Haluk Külah is with the Department of Electrical and Electronics Engineering, Middle East Technical University (METU), 06800 Ankara, Turkey, and also with the METU-MEMS Research and Application Center, 06800 Ankara, Turkey (e-mail: kulah@metu.edu.tr).

Color versions of one or more figures in this article are available at https://doi.org/10.1109/TCSI.2021.3053503.

Digital Object Identifier 10.1109/TCSI.2021.3053503

I. Introduction

PORTABLE electronic devices connected to a common network have become ubiquitous owing to the growth in intelligent machine-to-machine interfaces. Although energy consumption of such systems has drastically shrunk in the last decade, they still rely on bulky batteries for reliable operation. Considering their limited capacity and lifespan, batteries need to be charged or replaced for the sake of operation continuity; however, this may not be achievable in some applications due to location of the device [1] or extensive maintenance cost [2]. Energy scavenging provides an opportunity to power wireless sensor networks (WSNs) while eliminating usage of ponderous batteries. Harvesting energy from ambient sources can be carried out with thermal, vibrational, photovoltaic, or RF methods [3], [4]. Energy harvesting from vibrations is prominent due to abundance of vibration sources in environment [5]. Piezoelectric energy harvesters (PEHs) are broadly preferred transducers to convert mechanical vibrations into electrical energy as they possess superior output voltage and power levels, and are relatively easy to integrate compared to other vibration based harvesters [6]. MEMS technology plays an important role in fabrication of PEHs since it paves the way for miniaturization in complete harvesting systems and helps realizing self-sustained medical devices [7], [8]. PEHs generate AC voltage, which obstructs their usage to power up electronic loads directly in WSNs. Therefore, an interface circuit is utilized for AC/DC conversion and voltage regulation. Full bridge rectifier (FBR) and active doubler are common AC/DC converters owing to their simplicity [9], [10]. Nonetheless, their performance suffers from small inherent PEH capacitance that needs to be charged up to the level of output load voltage before charge transfer can start. Voltage drops across diodes in standard rectifiers significantly reduce power conversion efficiency, especially in micro-power generators.

Various nonlinear switching techniques have been developed as alternatives to improve output power [5], [11]. Synchronous electric charge extraction (SECE) technique utilizes an external inductor to extract and deliver energy to output load when deflection of PEH beam is at maximum [12]–[15]. SECE configuration with multiple bulky inductors proposed in [12] enhances power conversion efficiency over FBR without load dependence. To boost conversion efficiency further, multi-shot SECE technique was introduced to the literature in [6]. In this modified SECE, energy is extracted and transferred to the load with multi-stage process instead of a single one, which reduces conduction losses. Recently published SECE circuit in [14] is

optimized for shock type input excitations thanks to its ultra-low power control unit, but its performance gets worse for periodic PEH inputs. Another nonlinear switching technique called synchronized switch harvesting on inductor (SSHI) presented in [16]–[20] employs a large inductor to flip residual voltage on PEH capacitance in order to extend charging duration of the battery. Although the technique elicits superior output power and efficiency, SSHI performance strongly depends on loading conditions. A complete energy harvesting platform which combines MEMS PEH and SSHI circuit is presented in [17]. Relatively poor efficiency in voltage flipping limits power extraction improvement. SSHI rectifier proposed in [18] is capable of scavenging energy from both periodic and shock excitations. While the circuit incorporates maximum power point tracking (MPPT), both flipping operation in SSHI and DC/DC conversion in MPPT require external calibration of sub-units which prevents system autonomy. Reference [19] applies perturb and observe (P&O) method to a SSHI circuit to eliminate load dependence. However, it requires complex control and evaluation circuits for proper MPPT operation. A fundamental disadvantage of nonlinear switching methods based on SECE and SSHI is the requirement for external inductors in the range of mH's to attain favorable output power improvements and higher flipping efficiencies. Bulky inductors are responsible for most of the space occupied by harvesting interfaces, which limit harvesting application areas particularly in implantable micro-devices and hinder miniaturization.

Inductorless designs make use of switched capacitors (SCs) in piezoelectric harvesting circuits to flip residual voltage on PEH capacitance, as in the case of SSHI schemes [8], [21], [22]. Du and Seshia [21] uses 8 off-chip capacitors and 17 integrated power switches to implement synchronized switch harvesting on capacitor (SSHC) technique. The implementation reduces system volume since there are no external inductors. 8 external flipping capacitors matching in value to the PEH capacitance nevertheless enlarge system size and cost. Flipping-capacitor rectifier (FCR) proposed in [22] realizes a fully integrated implementation while employing on-chip capacitors and synchronous switches. However, the solution only applies to inherent PEH capacitance in pF range and excitation frequency around 100 kHz. As environmental vibrations typically occur at much lower frequency range and intrinsic capacitances of conventional PEHs are in 1-100 nF band, this circuit has limited application. Latest SSHC circuit introduced in [8] benefits from split-electrode MEMS harvester structure that shrinks equivalent capacitance value required for flipping, and hence facilitates on-chip integration of external capacitors. Conversion efficiency and power extraction improvement are reduced, however, by significant switching power dissipation. Furthermore, loading conditions have high impact on output power level due to load dependence of current inductorless designs [8], [21], [22]. Both SSHI [16], [18], [19] and inductorless [8], [21], [22] design techniques require external calibrations to acquire optimal bias flipping and maximum output power. Unfortunately, these calibrations alter with PEH type and ambient excitation conditions. Synchronized harvesting on capacitor-inductor (SSHCI) proposed in [23] has superior output power and efficiency performance with optimum flipping time detection. In addition, it utilizes a low-profile (small in size) external inductor in the range of tens of μH's to implement bias flipping. However, this circuit cannot address all problems that SSHI and inductorless methods experience due to its load dependent architecture.

The aim of this work is to implement an autonomous low-profile (i.e. volumes occupied by external components are small) interface circuit and maximum power point tracking (MPPT) system to utilize harvested energy from low-coupled MEMS piezoelectric transducers, and power up WSNs and biomedical devices. Interface system presented here is a recently fabricated IC based on SSHCI technique previously presented in [23] with improvements to enhance performance. In contrast to SSHI and inductorless designs, optimal charge flipping monitoring blocks inspired from active diode structures help SSHCI circuit to achieve fully autonomous operation without external intervention. Unique two-step voltage flipping operation facilitates utilization of low-profile inductor-capacitor components to shrink system volume and concurrently improve voltage flipping efficiency. A novel MPPT circuit is cascaded with SSHCI to lower load dependence. Refresh unit incorporated inside MPPT adds the ability to adjust optimum storage voltage with respect to variations in PEH excitation conditions. This unit makes SSHCI-MPPT circuit stand out among other interfaces in the literature. Moreover, inductor sharing concept is employed between SSHCI and MPPT blocks to reduce the number of external components. Section II introduces SSHCI-MPPT operation principles with theoretical optimal storage voltage calculation. Implementation details are given in section III. Experimental results of the fabricated ICs and performance comparison with state-of-the-art are included in section IV. Finally, section V provides a conclusion to the paper.

II. SSHCI-MPPT Interface Circuit

Fig. 1 depicts the proposed energy harvesting system with required external components. It is composed of SSHCI circuit utilizing a flipping inductor in the range of μH's, an original MPPT circuit, and a conventional low-dropout (LDO) regulator. PEH capacitance, L_{EXT}, and C_{EXT} create LC resonance circuit to achieve two-step voltage flipping, through which residual charge on PEH capacitance is inverted. A cold start-up is also included in SSHCI enabling system to charge the load from 0 V. R_D and C_D are delay components that control shorting pulse duration of PEH capacitance in one of the operation phases. Internally generated reference voltage levels are adjusted through R_{BIAS}. MPPT circuit shares the inductor with SSHCI for reduced cost. Capacitors C_{SENSE1} and C_{SENSE2} store piezoelectric open circuit voltage amplitude in order to determine optimal storage voltage. C_{REFR} governs piezoelectric open circuit voltage sampling frequency to compensate for leakage on C_{SENSE1} and C_{SENSE2}. R_{EXT1} and R_{EXT2} provides a fraction of storage voltage V_{STOR} that is needed to evaluate whether or not V_{STOR} is at optimum level. LDO regulator was added for the sake of system completeness. If needed, it provides desired regulated voltage levels (lower than V_{STOR} voltage) for electronic loads.

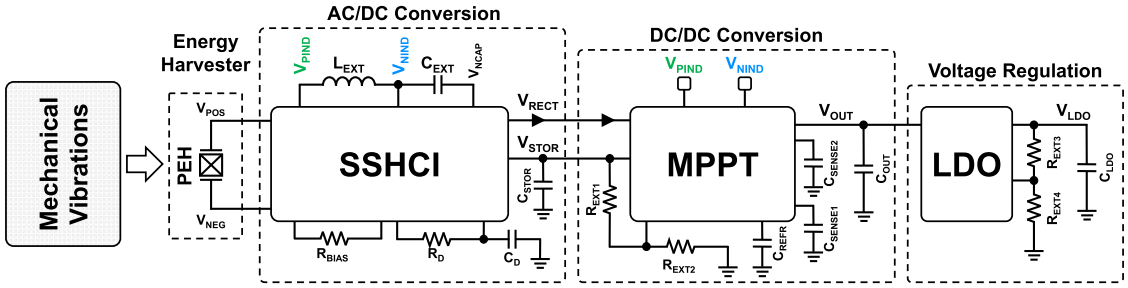

Fig. 1. Proposed low-profile energy harvesting interface system.

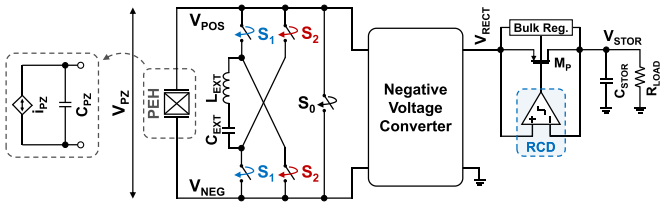

Fig. 2. Simplified circuit schematic of synchronized switch harvesting on capacitor-inductor (SSHCI) technique.

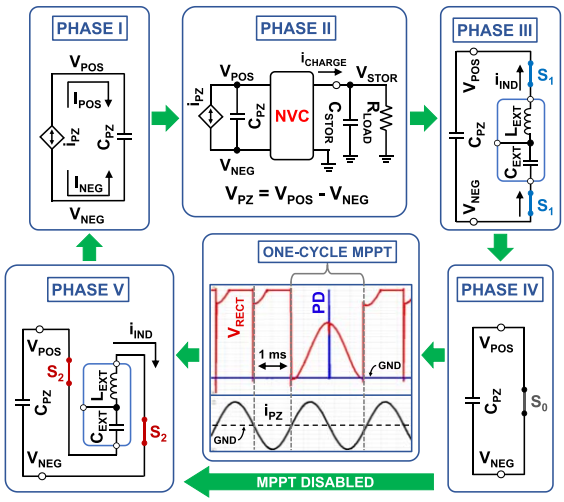

Fig. 3. Summary of SSHCI operation phases.

A. Operation Principle and System Architecture of SSHCI

Simplified SSHCI circuit schematic is illustrated in Fig. 2. Main SSHCI (or SSHCI-Only) operation has five phases that are shown in Fig. 3. If MPPT circuit is enabled, an extra phase occurs once in 20-50 periods of PEH swing (adjustable) between phase IV and V to sense piezoelectric open circuit voltage. This section focuses on SSHCI operation principles and SSHCI system architecture. Details of how MPPT works coherently with SSHCI are presented in section II.C.

Operation of SSHCI can be described as follows: Ambient vibrations lead to deflection on cantilever beam, which converts mechanical stress into electrical energy due to piezoelectric coating. During energy conversion process, electrical charge is accumulated on PEH intrinsic capacitance C_{PZ} (Phase I). Built-up AC voltage on C_{PZ} due to charge accumulation is henceforth rectified through the negative voltage converter (NVC). At the instant when rectified piezoelectric voltage V_{RECT} surpasses storage voltage V_{STOR}, charging of storage capacitor C_{STOR} through transistor M_P is started by reverse current detector (RCD), and system goes into phase II. RCD ends charging process when V_{RECT} recedes below V_{STOR}, and enables charge flipping detectors (CFDs) which will be explained in the next paragraph. S_1 power switches turn ON to transfer residual charge on C_{PZ} to external flipping capacitor C_{EXT} during phase III ($C_{EXT} = C_{PZ}$ for maximum energy transfer). When there is no charge to transfer from C_{PZ} to C_{EXT}, CFDs turn S_1 switches OFF. Then, PEH terminals are shorted via S_0 switch to nullify any remaining charge on C_{PZ} after energy transfer (phase IV). In phase V, temporarily stored charge on C_{EXT} is delivered back to C_{PZ} in reverse polarity to complete two-step flipping. At this time, again CFDs in use control flipping process through S_2 switches. Upon completion, SSHCI circuit to go back to phase I and disposes of any residual charge on external components. Fig. 4(a) depicts simulation waveforms of V_{PZ}, V_{STOR}, inductor current i_{IND}, and C_{PZ} shorting pulse observed during operation.

Fig. 4(b) presents system architecture of proposed SSHCI circuit which also indicates off-chip components. SSHCI has ten sub-units. Their functions will be described here. However, implementation details of sub-circuits will be provided in section III. Negative voltage converter (NVC) aims to rectify AC piezoelectric voltage V_{PZ}. NVC used in this system is the same active structure as in [23]. NVC is cascaded with an active diode structure that is composed of reverse current detector (RCD) and transistor M_P. This reduces the forward voltage drop on charging path, compared to full and half bridge rectifiers, down to a few tens of millivolts [24]. Start-up circuit monitors V_{STOR} voltage during colds start-up operation where C_{STOR} is charged through NVC and D_S. When there exists enough charge on C_{STOR}, signal EN_{TRIG} is generated to activate SSHCI. Optimum time intervals to transfer energy between C_{PZ} and C_{EXT} are autonomously detected using charge flipping detectors (CFDs) in phases III and V. CFDs communicate with switch control block utilizing CFD_1 (generated at the end of phase III) and CFD_2 (generated at the end of phase V) signals. Sign Detector (SD) informs SSHCI circuit about polarization of PEH terminals (V_{POS}>V_{NEG} or V_{POS}<V_{NEG}). This is important for SSHCI operation since SD output determines which CFD will be active in phases III and V. Shorting pulse generator (SPG), which has a structure similar to [25], determines duration of phase IV (C_{PZ} shorting phase). It is possible to adjust generated pulse width using R_D and C_D. Inductor oscillation cancellation (IOC) and residual charge elimination (RCE) blocks are high voltage transistors which remove any leftover charge on L_{EXT} and C_{EXT} after charge flipping phases finish. IOC shorts L_{EXT} terminals in phases I, II, and IV whereas

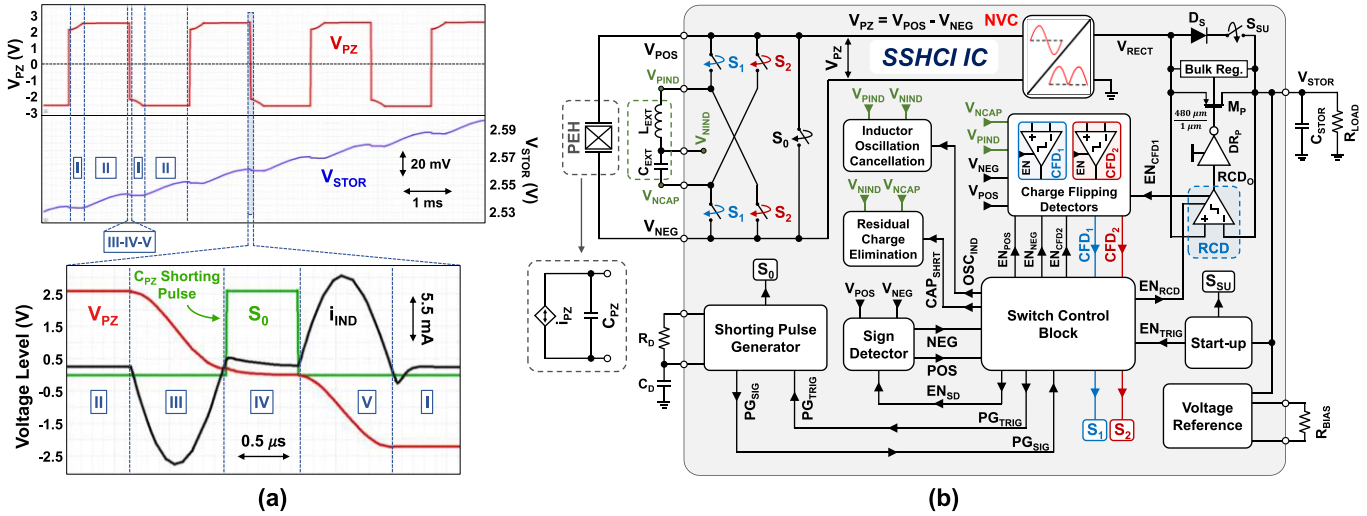

Fig. 4. (a) Simulation waveforms of piezoelectric voltage V_{PZ}, storage voltage V_{STOR}, inductor current i_{IND}, and C_{PZ} shorting pulse observed during operation. (b) System architecture of proposed SSHCI circuit showing on-chip and off-chip components.

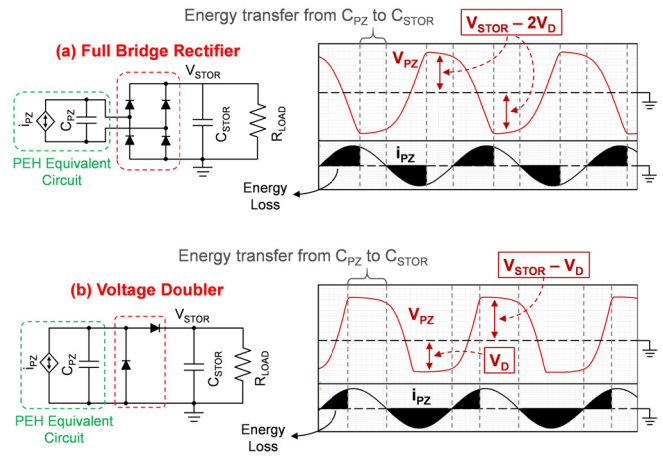

Fig. 5. (a) Schematic of conventional full bridge rectifier and (b) voltage doubler circuits and their corresponding simulation waveforms.

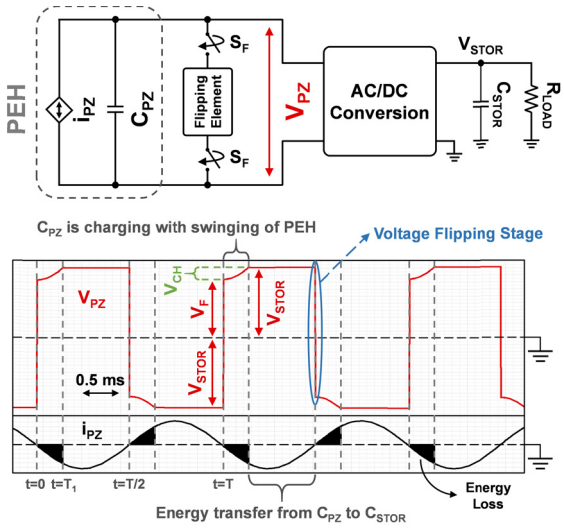

Fig. 6. Schematic of conventional SSH circuit, simulation waveforms of piezoelectric voltage V_{PZ} and piezoelectric current i_{PZ}.

RCE connects C_{EXT} terminals to each other during phases I and II. An internal reference circuit provides various voltage levels to bias SSHCI-MPPT. Biasing voltage levels can be tuned externally via R_{BIAS}.

B. Optimum Voltage Calculation

Energy extracted from PEH while using synchronized switch harvesting (SSH) technique is inevitably load dependent. This fact is not contingent upon the particular type of charge flipping component employed in various schemes, such as the capacitor in SSHC, the inductor in SSHI, or both in SSHCI. It is analytically derived in here that stored voltage, V_{STOR}, can be optimized to yield the highest power extraction in each system configuration. Power efficiency of the system depends on output power provided by the harvesting interface circuit. SSH circuits have superiority over other conventional methods in terms of output power. This fact is conceptually visualized in Fig. 5 and Fig. 6. Full bridge rectifier (FBR) and voltage doubler (VD) schematics and their corresponding simulation waveforms are depicted in Fig. 5 where black shaded areas represent energy loss in the useful input energy region. Due to voltage drops on diodes (V_D is diode ON voltage), both FBR and VD cannot deliver all charge to C_{STOR} and shaded energy loss regions occur. Moreover, V_{PZ} voltage needs to be charged to some point (V_{STOR}–$2V_D$ for FBR and $V_{STOR} - V_D$ for VD) before energy transfer to C_{STOR} starts and this reduces charging duration of C_{STOR} [16]. SSH circuits (SSHI, SSHC, and SSHCI) enlarge C_{STOR} charging duration with their voltage flipping operation and shrink energy loss areas as illustrated in Fig. 6. They make use of a negative voltage converter (NVC) cascaded with an active diode structure to eliminate diode voltage drops and thus boost power efficiency (Fig. 2).

MEMS PEH that is used to verify functionality and performance of the harvesting interface circuit has low piezoelectric coefficient and weak electromechanical coupling as in [8]. This means not all of mechanical vibrations are converted into electrical energy and generated voltage on PEH terminals affects mechanical vibrations very slightly, that is, the synchronized

switch damping effect mentioned in [26], [27] is ignored [8], [21], [28], [29]. Therefore, PEH can be modeled with intrinsic piezoelectric capacitance C_{PZ} parallel with excitation dependent current source i_{PZ} as shown in Fig. 6 [21]. i_{PZ} can be described by $i_{PZ} = I_0 \sin(\omega t)$, where I_0 and $\omega{=}2\pi f_{EX}$ are excitation amplitude and frequency of PEH, respectively. Produced charge by PEH over half a period of i_{PZ} oscillation with external vibrations can be calculated as follows:

$$Q_{\text{TOTAL}} = \int_0^{T/2} I_0 \sin(\omega t) dt = \frac{2I_0}{\omega} = 2V_{OC,P}C_{PZ}, \quad (1)$$

where $V_{OC,P}$ is the amplitude of piezoelectric open circuit voltage. Nonlinear switching methods like SSH try to transfer as much of this total charge as possible to output load. Although SSH operation flips most of residual charge after energy transfer to load, a flipping loss exists as represented by V_{CH} in Fig. 6, and some amount of generated charge on PEH is consumed to compensate for this loss. Therefore, net electrical charge transferred to storage capacitance C_{STOR} when PEH is connected to SSH circuit is:

$$Q_{NET} = 2V_{OC,P}C_{PZ} - (V_{STOR} - V_F)C_{PZ}, \quad (2)$$

where V_F is the flipped voltage magnitude after charging. If V_{STOR} does not change significantly in half period of i_{PZ} oscillation, extracted output power can be calculated as:

$$P_{NET} = \frac{V_{STOR}Q_{NET}}{T/2} = 2f_{EX}C_{PZ}V_{STOR} \times \left(2V_{OC,P} - V_{STOR} + V_F\right), \quad (3)$$

where f_{EX} is the periodic excitation frequency of PEH. V_F voltage is related with V_{STOR} as given in equation (4):

$$\eta_F = \frac{V_F + V_{STOR}}{2V_{STOR}} \Leftrightarrow V_F = V_{STOR}(2\eta_F - 1), \quad (4)$$

where η_F is defined as flipping efficiency. If we assume that flipping element in Fig. 6 is an inductor, we will achieve synchronized switch harvesting on inductor (SSHI) operation and according to [21], [30], the flipped voltage magnitude (V_{F-SSHI}) obtained after charging can be expressed as:

$$V_{F-SSHI} = \lambda V_{STOR} = V_{STOR}e^{-\frac{\pi}{2Q}} = V_{STOR}e^{-\frac{\pi}{\sqrt{\frac{4L_{EXT}}{R^2C_{PZ}}}}}, \quad (5)$$

where L_{EXT} is the external flipping inductor used in SSHI operation, C_{PZ} is the inherent piezoelectric capacitance, and R is total resistance of the loop RLC loop formed by S_F switches in Fig. 6. $\lambda = exp(-\pi/2Q)$ represents the fraction of the voltage maintained on the capacitor of an RLC circuit (Fig. 6) with quality factor $Q = \sqrt{L_{EXT}/(R^2C_{PZ})}$ after half cycle of damped resonance period [30]. It is possible to indicate flipping efficiency η_{F-SSHI} in terms of L_{EXT}, C_{PZ}, and R as given in equation (6). To increase flipping efficiency, L_{EXT} should be enlarged or R and C_{PZ} should be shrunk. Unlike SSHI, SSHCI employs a low-profile L_{EXT} in series with an external capacitor C_{EXT} as flipping elements ($C_{EXT} = C_{PZ}$). RLC loops established during phases III and V of SSHCI operation, shown in Fig. 3, reduce the equivalent capacitance of the loop since C_{EXT} and C_{PZ} are connected in series. Considering two consecutive voltage flipping steps occurring in phases III and V, the flipped voltage magnitude of SSHCI is $V_{F-SSHCI} = \lambda^2 V_{STOR}$ with $Q_{SSHCI} = \sqrt{L_{EXT}/(R^2(C_{PZ}/2))}$. Hence $\eta_{F-SSHCI}$ can be provided as:

$$\eta_{F-SSHI} = \frac{e^{-\frac{\pi}{\sqrt{\frac{4L_{EXT}}{R^2C_{PZ}}}}} + 1}{2} \& \eta_{F-SSHCI} = \frac{e^{-\frac{\pi}{\sqrt{\frac{2L_{EXT}}{R^2C_{PZ}}}}} + 1}{2}. \quad (6)$$

Combining equations (3) and (4), one can obtain:

$$P_{NET} = 4f_{EX}C_{PZ}V_{STOR}(V_{OC,P} + V_{STOR}[\eta_F - 1]). \quad (7)$$

To find optimum storage voltage for maximum output power, derivative of P_{NET} with respect to V_{STOR} is set equal to zero:

$$\frac{dP_{NET}}{dV_{STOR}} = 0 = 4f_{EX}C_{PZ}V_{OC,P} + 8f_{EX}C_{PZ}V_{STOR,OPT}(\eta_F - 1), \quad (8)$$

$$V_{STOR,OPT} = \frac{V_{OC,P}}{2(1 - \eta_F)}. \quad (9)$$

Equation (9) is calculated under the assumption that there is no voltage drop at AC/DC conversion stage [8]. If voltage drop exists on the charging path, optimum storage voltage $V_{STOR,OPT}$ will be less than the one given by expression (9). Furthermore, this calculation is true for low electromechanically coupled PEHs under purely sinusoidal vibrations [31], which are good assumptions for the targeted PEH and operating conditions.

TABLE I
THEORETICAL MAXIMUM OUTPUT POWER EXPRESSIONS FOR VARIOUS HARVESTING INTERFACE CIRCUITS

Full Bridge Rectifier (FBR)	$P_{FBR} = C_{PZ}(V_{OC,P} - 2V_D)^2 f_{EX}$
Voltage Doubler (VD)	$P_{VD} = C_{PZ}(V_{OC,P} - V_D)^2 f_{EX}$
Synchronous Electric Charge Extraction (SECE)	$P_{SECE} = C_{PZ}{V_{OC,PP}}^2 f_{EX}$
Synchronized Switch Harvesting (SSH)	$P_{SSH} = \frac{C_{PZ}{V_{OC,P}}^2 f_{EX}}{1 - \eta_F}$

Table I presents theoretical maximum output power expressions of FBR [16], voltage doubler [10], [16], and SECE [32] which are well studies in the literature. Furthermore, if we substitute for optimum storage voltage $V_{STOR,OPT}$ expression (9) into equation (7), we can achieve P_{SSH} expression for the maximum output power of synchronized switch harvesting (SSH) based techniques (SSHI, SSHC, and SSHCI). Utilizing these equations, P_{OUT}/P_{FBR} plots of different energy harvesting interface circuits for different piezoelectric open circuit voltage levels ($V_{OC,P}$) were depicted in Fig. 7. It is clear that both nonlinear switching techniques SECE and SSH outperforms FBR and voltage doubler (VD). Even though SECE performs better than SSH technique for voltage flipping efficiency, η_F, of 50-70%, SSH delivers more output power when η_F is increased to 80%. That is because output power

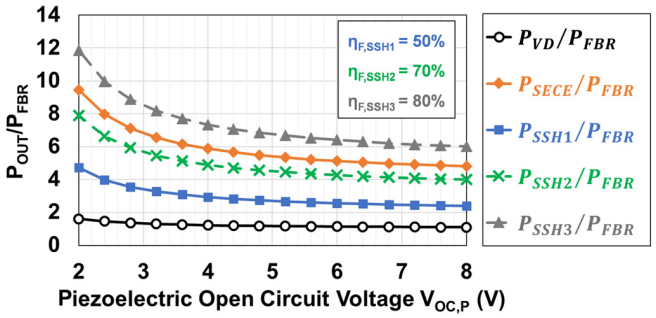

Fig. 7. Theoretical output power performance comparison of FBR, VD, SECE, and SSH techniques. SSH power is plotted for three different flipping efficiencies $\eta_{F,SSH1} = 50\%$, $\eta_{F,SSH2} = 70\%$, and $\eta_{F,SSH3} = 80\%$.

highly depends on η_F as indicated by equation (7). As η_F increases, energy loss shown in Fig. 6 reduces, which leads to improved power efficiency.

C. MPPT Concept

MPPT circuit in Fig. 8(a) targets optimum V_{STOR} voltage. It samples $V_{OC,P}$ value once in 20-50 periods of PEH swing (configurable), and compares it with a fraction of V_{STOR} which is obtained by resistor division using R_{EXT1} and R_{EXT2}. It is important to note that the same inductor L_{EXT} appearing in SSHCI voltage flipping operation is utilized here.

Simulation waveforms obtained during one-cycle $V_{OC,P}$ sensing are provided in Fig. 8(b-d). One-cycle sensing starts when MPPT circuit is enabled via refresh unit or external enable signal. However, one-cycle $V_{OC,P}$ sensing does not start immediately in order not to disturb SSHCI phases and cause misleading $V_{OC,P}$ storage. Once phase IV of SSHCI (in which C_{PZ} is shorted after energy transfer to eliminate any residuals) finishes as shown in Fig. 8(c), system lets PEH to accumulate charge on C_{PZ} with swinging of cantilever beam. The instant, at which AC voltage on C_{PZ} reaches its maximum, is caught by peak detector (PD). This maximum also corresponds to peak-to-peak piezoelectric open circuit voltage $V_{OC,PP}$. Thanks to switches S_{MPP1}, S_{MPP2}, and S_{MPP3} controlled by pulse generators, piezoelectric open circuit voltage amplitude $V_{OC,P}$ is stored on C_{SENSE2}. These three switches work in harmony as follows: At the end of SSHCI phase IV, both S_{MPP1} and S_{MPP3} turn ON to dispose of charge on sensing capacitors C_{SENSE1} and C_{SENSE2}. This process sets up C_{SENSE1} and C_{SENSE2} for the upcoming $V_{OC,P}$ storage. When peak detection signal arrives, S_{MPP1} and S_{MPP3} turn OFF and S_{MPP2} turns ON to sample $V_{OC,PP}$ value onto C_{SENSE1}. After a short time, S_{MPP2} turns OFF while S_{MPP3} turns ON to share charge between C_{SENSE1} and C_{SENSE2}. Since $C_{SENSE1} = C_{SENSE2} = 33$ pF, charge is shared equally and $V_{OC,P}$ is stored on both of them. This is because hysteresis comparator in Fig. 8(a), which compares fraction of storage voltage $V_{STOR-DIV}$ and $V_{OC,P}$, is designed and optimized to compare voltage levels near and below half of the storage voltage V_{STOR}. It is hence aimed to decrease power consumption of the hysteresis comparator which is mostly ON after MPPT operation is enabled. Furthermore, comparing $V_{OC,P}$ level instead of $V_{OC,PP}$ reduces the risk of operational problems in case $V_{OC,PP}$ drifts beyond the optimal common mode range of the comparator. After charge sharing between C_{SENSE1} and C_{SENSE2}, S_{MPP3} turns OFF. One-cycle $V_{OC,P}$ sensing process is finalized when V_{RECT} reaches zero, and the moment V_{RECT} becomes zero also corresponds to $i_{PZ} \approx 0$. As it can be seen from the simulation result in Fig. 3, the time interval between two zero voltage crossings of V_{RECT} represents almost one full cycle of i_{PZ} oscillation which, in turn, indicates one PEH excitation period. Zero-crossing detectors (ZCDs) which generate $MPPT_{FIN}$ signal detect zero crossing instant and SSHCI continues from where it is left as depicted in Fig. 8(d).

Following one-cycle $V_{OC,P}$ sensing, hysteresis comparator in Fig. 8(a) is enabled, which checks whether $V_{STOR,OPT}$ is reached. Instead of comparing V_{STOR} with its optimum value $V_{STOR,OPT}$, MPPT circuit actually compares fraction of V_{STOR} (which is $V_{STOR-DIV}$) with $V_{OC,P}$ to achieve $V_{STOR,OPT}$. Resistor divider established by R_{EXT1} and R_{EXT2} generates $V_{STOR-DIV}$. Hysteresis comparator in Fig. 8(a) regulates $V_{STOR-DIV}$ to $V_{OC,P}$ voltage level ($V_{STOR-DIV} \approx V_{OC,P}$) by initiating DC/DC conversion operation through switches S_3, S_4, and S_5. Once voltage flipping efficiency η_F is known (η_F depends on L_{EXT}, C_{PZ}, and R but not on different excitation conditions), R_{EXT1} and R_{EXT2} can be adjusted to let system attain $V_{STOR,OPT}$. Voltage division provides:

$$V_{STOR}\frac{R_{EXT2}}{R_{EXT1}+R_{EXT2}} = V_{STOR-DIV} \cong V_{OC,P} \Leftrightarrow \frac{V_{STOR}}{V_{OC,P}} = \frac{R_{EXT1}+R_{EXT2}}{R_{EXT2}}. \quad (10)$$

If optimum storage voltage $V_{STOR,OPT}$ expression from equation (9) is substituted for V_{STOR} in (10), one can obtain:

$$\frac{R_{EXT1}}{R_{EXT2}} = \frac{1}{2(1-\eta_F)} - 1. \quad (11)$$

Equation (11) governs R_{EXT1}/R_{EXT2} ratio to keep storage voltage at its optimum value ($V_{STOR,OPT}$). Therefore, once η_F is obtained through measurement, R_{EXT1}/R_{EXT2} ratio can be tuned based on equation (11) to attain $V_{STOR,OPT}$. At the end of one-cycle $V_{OC,P}$ sensing, a fraction of optimum storage voltage $V_{STOR,OPT}$ is generated at negative input terminal of the hysteresis comparator (on C_{SENSE2} capacitor), and is equal to $V_{OC,P}$. Since R_{EXT1}/R_{EXT2} ratio is determined according to equation (11), $V_{STOR-DIV}$ becomes equal to $V_{OC,P}$ as V_{STOR} reaches $V_{STOR,OPT}$. If V_{STOR} voltage is less than $V_{STOR,OPT}$ at the end of one-cycle $V_{OC,P}$ sensing, hysteresis comparator lets V_{STOR} voltage increase by not creating any charging path from C_{STOR} to C_{OUT}. During that time, SSHCI operation continues and V_{STOR} goes up with swinging of PEH as described in section concerning the operation principle of the SSHCI circuit. When $V_{STOR} > V_{STOR,OPT}$, which means $V_{STOR-DIV} > V_{OC,P}$, hysteresis comparator triggers a DC/DC conversion through power switches S_3, S_4, and S_5. During that time, amount of charge which is transferred from C_{STOR} to C_{OUT} and this duration is determined by adjustable pulse generator similar to the one proposed in [25]. This pulse generator inside MPPT switching control block directly governs how much time S_3 stays ON.

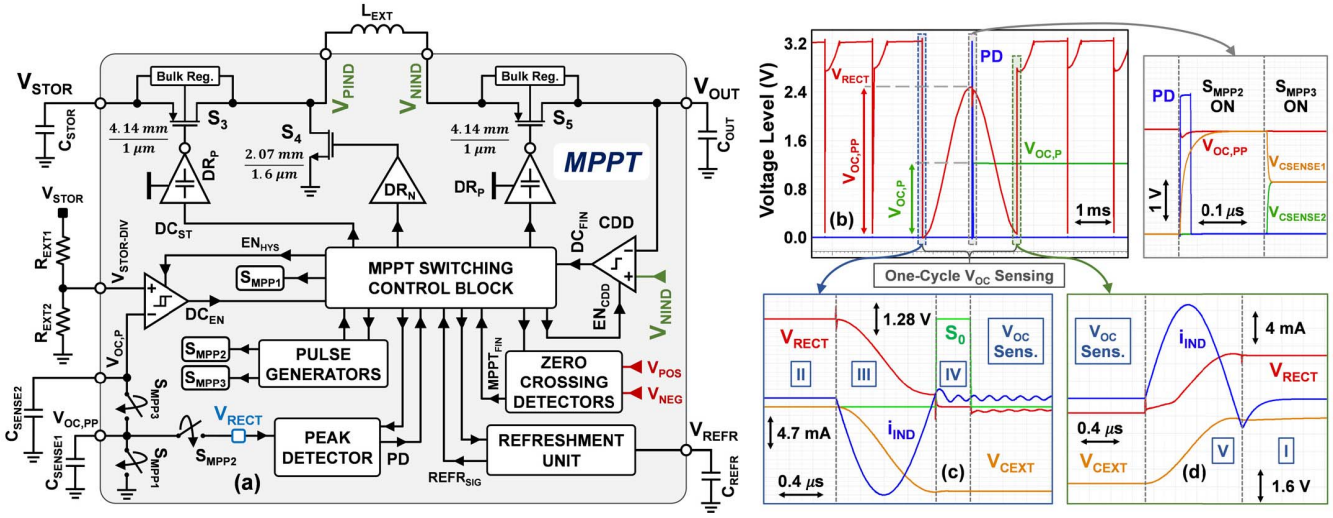

Fig. 8. (a) Schematic of one-cycle $V_{OC,P}$ sensing MPPT circuit. Simulation waveforms of (b) one-cycle $V_{OC,P}$ sensing and SSHCI operation phases when sensing (c) starts and (d) ends. V_{RECT} is the rectified piezoelectric voltage, PD is the output of peak detector, $V_{OC,PP}$ is the peak-to-peak piezoelectric open circuit voltage, i_{IND} is the current passing through L_{EXT}, and V_{CEXT} is the voltage stored on external flipping capacitor C_{EXT}.

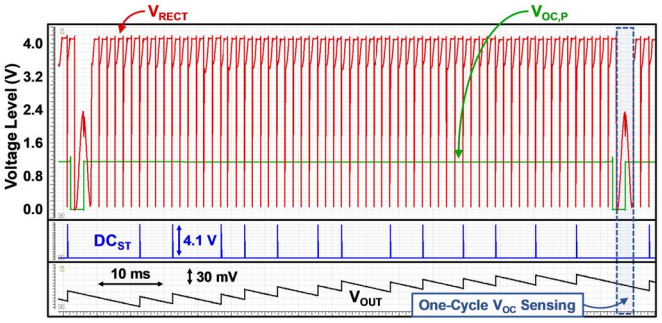

Fig. 9. Simulation result of output load charging and refresh operations that occur in MPPT. V_{RECT} is the rectified piezoelectric voltage, V_{OUT} the is output load voltage, $V_{OC,P}$ is the stored piezoelectric open circuit amplitude and DC_{ST} is the control signal of switch S_3.

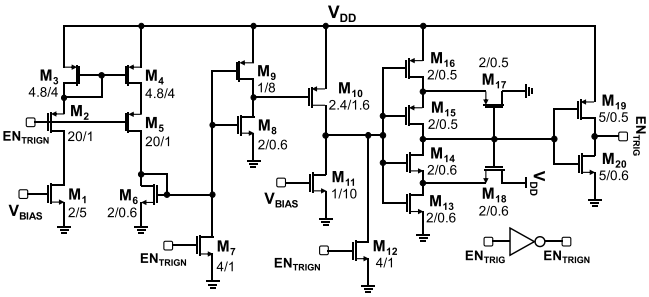

Fig. 10. Schematic of start-up trigger circuit.

Energy is delivered to C_{OUT} over L_{EXT}, S_3, and S_5. When pulse ends, S_3 turns OFF and S_4 starts operating, which enables the system to extract residual energy on L_{EXT}. Charge depletion detector (CDD), which is a high-speed comparator, monitors terminals of switch S_5 and creates a signal to break charging path if V_{OUT} becomes larger than V_{NIND}. This finalizes one DC/DC conversion cycle and hysteresis comparator is enabled again to observe V_{STOR} level. All of the switches S_3, S_4, and S_5 are required in MPPT circuit since they make inductor sharing action possible by isolating external inductor L_{EXT} from MPPT circuit when it is not in use. The same external inductor L_{EXT} is also employed in SSHCI flipping process and switches S_3, S_4, and S_5 prevent possible coupling between voltage flipping process in SSHCI and DC/DC conversion in MPPT circuits. Fig. 9 presents a simulation result summarizing output load charging and refresh operations that take place in MPPT. Refresh unit provides signals to conduct one-cycle $V_{OC,P}$ storage once in at least 20 periods of PEH swing. It facilitates proper MPPT operation by keeping $V_{OC,P}$ value on C_{SENSE2} fresh. Refresh unit prevents degradation of stored voltage due to leakage. Moreover, it helps MPPT system adapt to changes at $V_{OC,P}$ level. Frequency of refreshing depends on the value of C_{REFR}.

In case V_{STOR} does not reach $V_{STOR,OPT}$ level due to some reasons (e.g., external loading on V_{STOR} node is present), DC/DC conversion operation will not start and only one-cycle $V_{OC,P}$ sensing will occur once in 20-50 periods of PEH swing until V_{STOR}>$V_{STOR,OPT}$ (also, main SSHCI operation will be active). The reason behind disabling DC/DC conversion for V_{STOR}<$V_{STOR,OPT}$ can be summarized as follows: For V_{STOR} levels less than $V_{STOR,OPT}$ (0<V_{STOR}<$V_{STOR,OPT}$), output power (P_{NET}) calculated previously in equation (7) increases as V_{STOR} goes up. Besides, MPPT system is not able to provide energy transfer from C_{OUT} to C_{STOR}. Therefore, DC/DC conversion operation will not be initiated until V_{STOR}>$V_{STOR,OPT}$. However, this does not create any problems for SSHCI-MPPT IC since nonlinear SSHCI technique will try to accumulate charge on C_{STOR} as much as possible and if there is no external resistive load (R_{LOAD}) directly connected to C_{STOR}, V_{STOR} will eventually become larger than $V_{STOR,OPT}$ at some point. Then, DC/DC conversion in MPPT circuit will begin to transfer energy from C_{STOR} to C_{OUT} as discussed previously.

Theoretical output power of SSHCI circuit is presented in equation (7). SSHCI-MPPT operation tries to keep V_{STOR} at its optimum value whose expression is provided in equation (9). Load resistance R_{LOAD} connected in parallel with output capacitor C_{OUT} does not affect output power calculated in equation (7). This is due to the fact that V_{STOR} is kept around

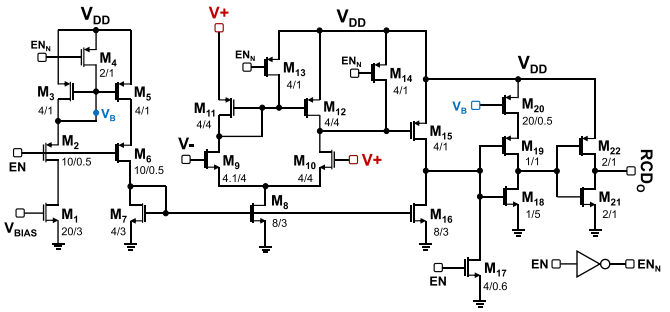

Fig. 11. Implementation of reverse current detector (RCD).

its optimum value by MPPT circuit and other parameters in equation (7), which are PEH excitation frequency f_{EX}, inherent piezoelectric capacitance C_{PZ}, piezoelectric open circuit voltage amplitude $V_{OC,P}$, and flipping efficiency η_F, do not depend on R_{LOAD}. If a dedicated MPPT circuit is not utilized, R_{LOAD} connected in parallel with C_{STOR} will change V_{STOR} and output power of SSHCI circuit calculated in (7) will henceforth vary depending on R_{LOAD}. Power dissipation of MPPT sub-circuits and switching losses reduce output power of SSHCI from its theoretical value.

III. Sub-Circuit Implementation Details

In this section, design of critical SSHCI-MPPT sub-block circuits in Fig. 4(b) and 8(a) are detailed.

A. Start-Up Trigger

Harvesting system is able to charge C_{STOR} from completely discharged condition (0 V) by means of NVC, on-chip diode D_S and switch S_{SU} as shown in Fig. 4(b). When adequate amount of charge is accumulated on C_{STOR}, RCD and SR latches in switching control block are enabled to sequence SSHCI phases. Start-up trigger circuit depicted in Fig. 10 generates the associated enable signal. As C_{STOR} charges from zero voltage with ambient motion, reference voltage levels are generated first for biasing. Then, as the supply voltage V_{DD} develops, the bias current increases, leading to charge accumulation on the node where gates of M_6, M_8, and M_9 transistors are connected. Voltage at this node activates the inverter made up of M_8 and M_9, and the generated signal EN_{TRIG} triggers SSHCI system. Start-up trigger circuit is disabled completely after the generation of EN_{TRIG} signal. The bias voltage V_{BIAS} controls the triggering voltage level.

B. Reverse Current Detector (RCD) and Optimal Charge Flipping Detection

For autonomous SSHCI operation, switch timing is controlled with reverse current detector (RCD) and a set of charge flipping detectors (CFDs). Hybrid 2-stage comparator topology in Fig. 11 is utilized to sustain high performance operation across the output voltage range for detecting charging intervals. Common gate configuration, facilitated by M_{11} and M_{12}, increases detection sensitivity of the instant when V_+ first drops below V_-. Since RCD is enabled during both phases I and II, its power dissipation has an utmost impact on system efficiency. Current limiting M_{20} reduces current drawn from

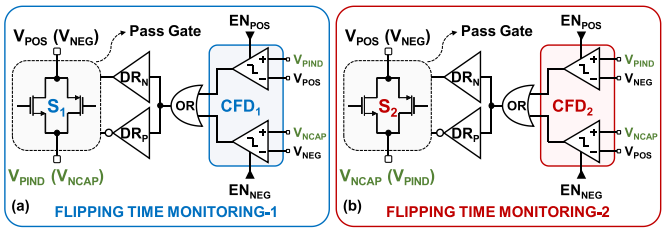

Fig. 12. Flipping time monitoring architectures constructed for (a) phase III and (b) phase V of SSHCI operation.

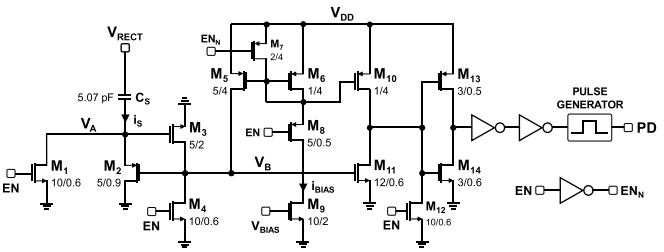

Fig. 13. Peak detector schematic.

supply voltage while RCD output transitions (i.e. detection instants).

Unlike [8], [18], [21] optimal charge flipping is achieved autonomously via flipping monitoring architecture detailed in Fig. 12. The scheme is based on comparison of different PEH terminals and external inductor-capacitor combination. P-input comparators are used to compare voltage levels below half of V_{STOR}, whereas N-input comparators detect input voltage crossings above $V_{STOR}/2$. Different comparator types ensure performance across a wide common mode range [23]. Comparators draw around 3 μA when they are activated and are strictly turned OFF when they are not operating. CFDs are more immune to input voltage offset than RCD since CFDs operate in saturation region. Nevertheless, precise tuning of biasing voltage is possible via R_{BIAS} resistor in reference circuit to compensate for voltage offsets.

C. Peak Detector and Refresh Unit

The circuit used as the peak detector in MPPT is originally proposed in [6] where circuit details are presented with relevant simulations and experimental results. Fig. 13 depicts the peak detector schematic. This circuit is capable of detecting voltage peaks across a wide frequency spectrum. Since the detector works in current mode, rectified piezoelectric voltage is transformed into current through on-chip capacitor C_S. While V_{RECT} rises, node voltage V_A increases up to the threshold voltage of M_3 due to negative feedback formed by M_2 and M_3. Sensing current i_S becomes zero as V_{RECT} reaches its peak value. Then, transistor M_3 turns OFF as a result of decreased voltage at node V_A. This process disables negative feedback loop, and voltage starts to develop at node V_B due to mirrored bias current. Common source amplifier, consisting of M_{10} and M_{11}, and a buffered output stage generates the peak detection pulse.

$V_{OC,P}$ voltage stored on external capacitor C_{SENSE2} drops slowly due to leakage through MOSFETs. This leads to an error in optimum storage voltage calculation in the circuit. One-cycle $V_{OC,P}$ storage refresh unit in Fig. 14(a) addresses

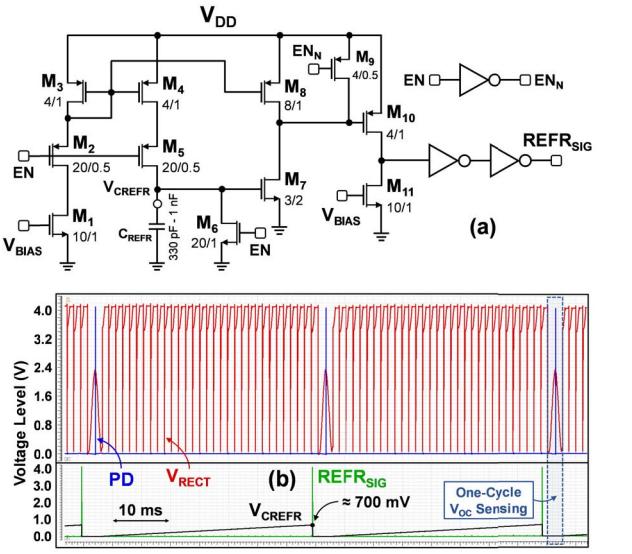

Fig. 14. (a) Schematic of one-cycle $V_{OC,P}$ storage refresh unit and (b) simulation waveforms of peak detector output (PD), refreshment trigger signal ($REFR_{SIG}$), voltage accumulated on external capacitance C_{REFR} (V_{CREFR}), and V_{RECT}.

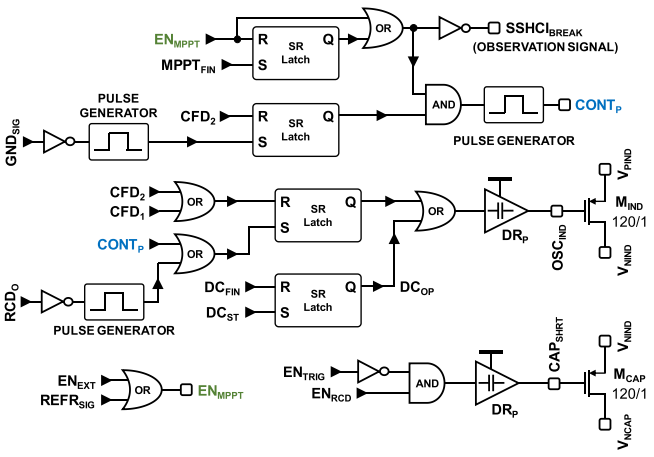

Fig. 15. Control unit implementation for inductor sharing and external flipping capacitor shorting signal.

this problem. After one-cycle $V_{OC,P}$ sensing, refresh unit is enabled, and mirrored biasing current begins to charge external capacitor C_{REFR}. When accumulated voltage V_{CREFR} reaches about 700 mV, transistor M_7 turns ON and triggers detection signal generation. M_7, M_8, M_{10}, and M_{11} constitute two-stage common source amplifier to expedite detection and provide high edge rate. Fig. 14(b) illustrates peak detection and one-cycle $V_{OC,P}$ sensing with corresponding detection signals.

D. Inductor Sharing Control

Fig. 15 presents the control unit implementation that makes inductor sharing possible between SSHCI and MPPT circuits. Signals generated in both SSHCI and MPPT operations are employed not to obstruct any switching mechanism where usage of external inductor is unavoidable.

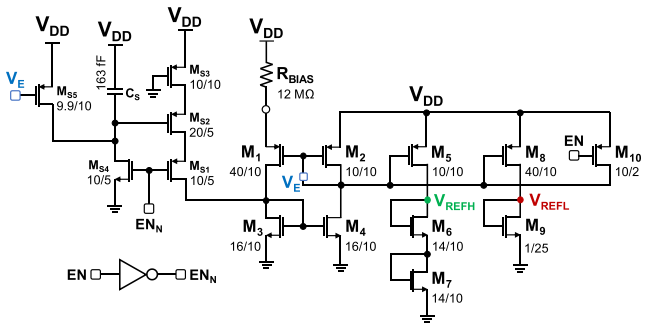

Fig. 16. Schematic of voltage reference circuit.

Control of external flipping capacitor C_{EXT} shorting signal, which drives M_{CAP}, is relatively simpler. Since C_{EXT} is utilized in flipping operation phases III, IV, and V, it can be managed by RCD enable signal. When RCD is active (EN_{RCD} is low), switch M_{CAP} shorts C_{EXT} terminals to eliminate any residual charge. During phases III, IV, and V, RCD is disabled and M_{CAP} is turned OFF, which allows C_{EXT} to be charged and discharged and facilitates low-profile voltage flipping. C_{EXT} is shorted when it is not used.

In SSHCI-Only operation where MPPT is disabled (EN_{MPPT} high), inductor oscillation cancellation signal OSC_{IND} is generated using RCD output RCD_O and adjustable C_{PZ} shorting pulse GND_{SIG} generated in phase IV. Charge flipping detection signals CFD_1 and CFD_2, established at the end of phases III and V, turn M_{IND} ON in order to remove residual charge and prevent oscillation throughout phases I, II, and IV. In cases where MPPT is enabled either with an external signal EN_{EXT} or refresh signal pulse $REFR_{SIG}$, $CONT_P$ signal holds SSHCI circuit from entering phase V until one-cycle $V_{OC,P}$ sensing is finished. Otherwise, DC/DC conversion in MPPT, provided by switches S_3, S_4, and S_5, uses inductor L_{EXT} when DC_{ST} signal is generated as shown in Fig. 9. DC/DC conversion is terminated with DC_{FIN} signal, which is produced by charge depletion detector (CDD). M_{IND} shorts L_{EXT} when not in use to avoid any oscillations.

E. Voltage Reference

Fig. 16 depicts proposed voltage reference circuit, which is a modified version of PTAT bias-current generator presented in [15]. Voltage on resistor R_{BIAS} is created due to gate-source voltage difference between M_1 and M_2. M_3 and M_4 regulate the current passing through M_1 and M_2 to be equal at biasing current level. This supply independent current is mirrored through M_5 and M_8, and is then converted into reference voltage through saturated load MOSFETs M_6, M_7, and M_9. M_{S1}-M_{S5} and C_S serve as start-up configuration. Generated reference levels V_{REFH} and V_{REFL} can be tuned via R_{BIAS}.

IV. Experimental Results

SSHCI-MPPT circuit, for which the die micrograph is depicted in Fig. 17, has been fabricated in 180 nm CMOS technology. The layout active area is 1400 μm $\times$ 880 μm without on-chip voltage reference and low-dropout regulator.

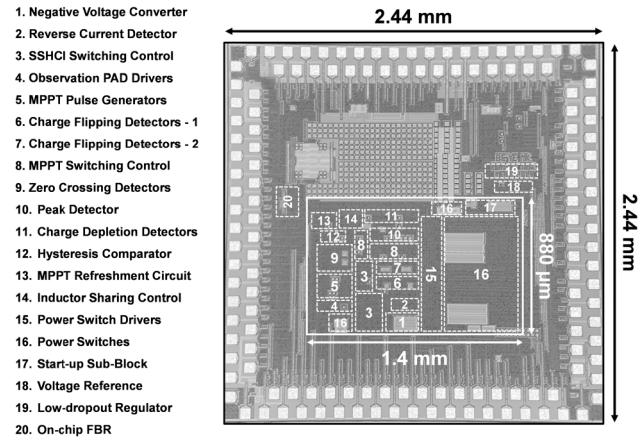

Fig. 17. Die micrograph of SSHCI-MPPT chip fabricated in 180 nm CMOS.

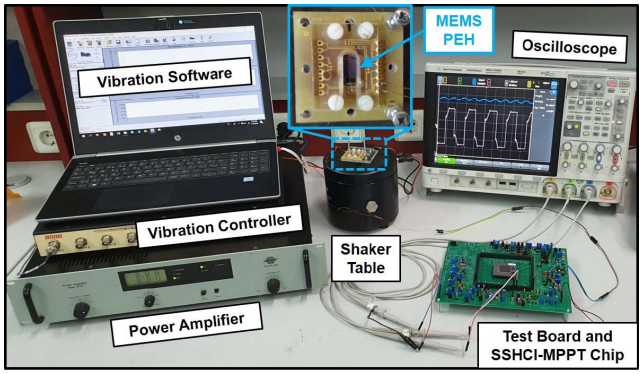

Fig. 18. Experimental setup for SSHCI-MPPT design validation.

TABLE II
LIST OF ALL OFF-CHIP COMPONENTS AND THEIR PARAMETERS

Component	Value	Size
L_{EXT}	68 µH & 100 µH	18 mm^3
C_{EXT}	2 nF	3.13 mm^3
C_D, C_{SENSE1}, C_{SENSE2}	33 pF	3 x 0.3 mm^3
C_{REFR}	330 pF – 1nF	1.1 mm^3
C_{STOR}	453 nF	28 mm^3
C_{OUT}	1 µF	6.1 mm^3
C_{LDO}	4.7 µF	8.2 mm^3
R_{BIAS}	12 MΩ	< 50 mm^3
R_D	29 kΩ	0.58 mm^3
R_{EXT1}	50 MΩ – 20 MΩ	Variable
R_{EXT2}, R_{EXT3}, R_{EXT4}	20 MΩ – 10 MΩ	Variable

Experimental setup used to evaluate performance of fabricated SSHCI-MPPT chip is illustrated in Fig. 18. A custom MEMS PEH with a footprint of 36 mm^2 is stimulated on a shaker table to charge a 453 nF storage capacitor C_{STOR} through the interface circuit. The PEH has an inherent capacitance, C_{PZ} of 2 nF and is excited at its resonance frequency of 415 Hz through a vibration setup that includes the shaker table, amplifier, controller, and vibration software. 68 and 100 μH SMD inductors have been utilized as L_{EXT} along with $C_{EXT} = C_{PZ} = 2$ nF to implement voltage flipping and DC/DC conversion operations. All off-chip components,

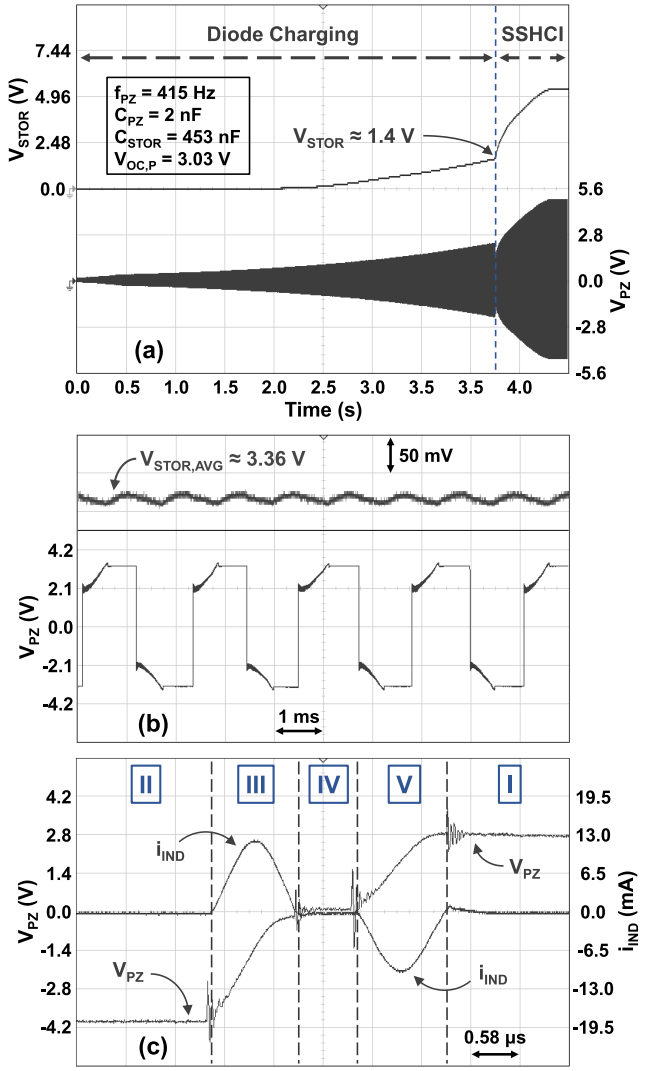

Fig. 19. Measured waveforms of piezoelectric voltage V_{PZ}, storage voltage V_{STOR}, and inductor current i_{IND} demonstrating (a) start-up, (b) C_{STOR} charging, and (c) two-stage voltage flipping operation in main SSHCI circuit.

their corresponding values, and sizes utilized during measurements are listed in Table II. External resistors R_{BIAS} and R_{EXT1}-R_{EXT4} may seem to dominate overall system volume. This is because through-hole resistors were utilized during experiments to achieve the best chip performance. After attaining optimum chip performance, resistors R_{BIAS}, R_{EXT1}-R_{EXT4}, and capacitor C_{STOR} can be selected from SMD components (with volume of each ≤ 10 mm^3) to shrink system volume further. External inductors employed in SSHI [18], [19] and SECE [12], [14] single-handedly occupy as large space as SSHCI-MPPT interface system. MEMS PEH takes up significantly less volume compared to discrete harvesters in [14], [18], [21], although it occupies most of the volume in the presented harvesting system.

Fig. 19(a) shows measured start-up operation made possible by NVC, on-chip diode D_S, and switch S_{SU}. V_{STOR} level required to activate SSHCI operation is determined by start-up trigger circuit in Fig. 10. Required V_{STOR} can be as low as 1.1 V; however, start-up trigger circuit was adjusted to generate the signal around 1.4 V to let SSHCI work safely.

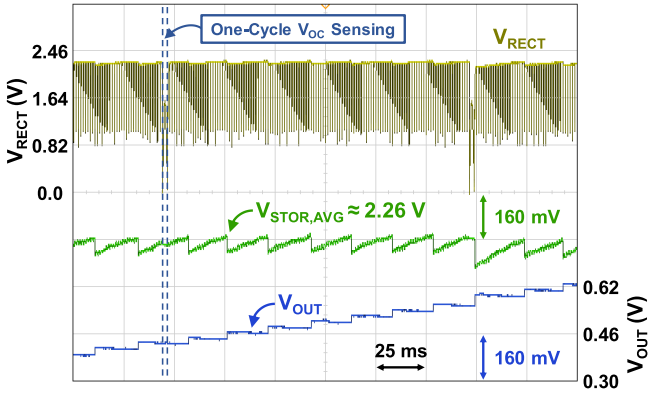

Fig. 20. Measured waveforms of V_{RECT}, V_{STOR}, and V_{OUT} during SSHCI-MPPT charging operation.

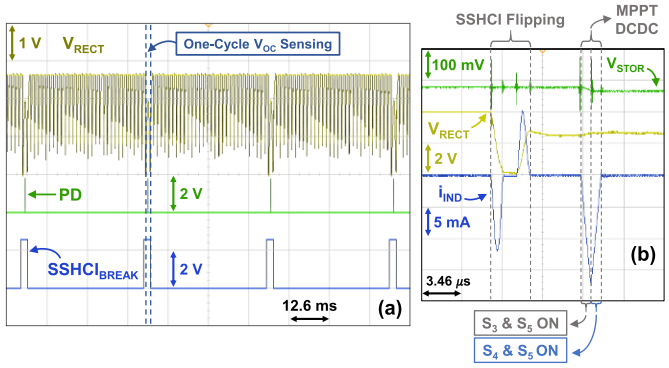

Fig. 21. Measured waveforms of V_{RECT}, V_{STOR}, V_{OUT}, i_{IND}, and control signals PD and $SSHCI_{BREAK}$ during (a) multiple one-cycle $V_{OC,P}$ sensing and refreshes, and (b) inductor sharing.

Fig. 19(b) presents measured SSHCI charging, while Fig. 19(c) depicts details of voltage flipping phases. SSHCI circuit does not require any external adjustment to accomplish storage capacitor charging and optimal charge flipping. It operates with low-profile external inductors and nevertheless provides flipping efficiency levels comparable to conventional SSHI circuits [16]–[18]. The waveforms in Fig. 19 represent validation of core SSHCI operation with MPPT circuit disabled. Fig. 20 illustrates measured waveforms with enabled MPPT for rectified piezoelectric voltage V_{RECT}, storage voltage V_{STOR} at the output of SSHCI stage, and load voltage V_{OUT}. As demonstrated, MPPT works seamlessly with SSHCI, and keeps V_{STOR} around 2.26 V for piezoelectric open circuit amplitude of $V_{OC,P}$ =0.81 V. Furthermore, two consecutive $V_{OC,P}$ sensing and output capacitance (C_{OUT} =1 μF) charging (blue line) operations are shown in the same figure (Fig. 20). Fig. 21(a) presents multiple $V_{OC,P}$ sensing and refreshes, which were realized by shrinking capacitor C_{REFR} to achieve multiple $REFR_{SIG}$ control signals depicted in Fig. 14. When $REFR_{SIG}$ is generated during system activity, it causes SSHCI operation to suspend after phase IV to let one-cycle $V_{OC,P}$ sensing to occur. $SSHCI_{BREAK}$ in Fig. 21(a) represents SSHCI suspension signal triggered by $REFR_{SIG}$. After one-cycle $V_{OC,P}$ sensing is finished, it goes to low and SSHCI continues its operation with second flipping in phase V. Fig. 21(b) depicts inductor sharing. SSHCI-MPPT system is capable of utilizing the same external inductor L_{EXT} to attain both voltage flipping and DC/DC conversion. Adjustable pulse generators inside MPPT switching control block in Fig. 8(a) govern S_3 ON duration and determine the amount of current passing through inductor in DC/DC conversion.

Fig. 22(a) and (b) depict measured output power of main SSHCI (or SSHCI-Only) operation under different excitation levels with disabled MPPT. At $V_{OC,P}$ =1.02 V excitation, SSHCI is able to attain 5.44 times relative output power performance improvement over harvested power of an ideal full bridge rectifier (FBR). Ideal FBR can be defined as a rectifier which has no voltage drop across its diodes and is able to provide theoretical maximum output power of $P_{IDEAL-FBR} = f_{EX} C_{PZ} V_{OC,P}^2$ [15], [16]. As excitation level is increased, relative performance enhancement decreases due to larger damping of PEH and increased conduction and switching losses (Fig. 22(b)). As illustrated by Fig. 22(c), maximum power conversion efficiency ($\eta = P_{STOR}/P_{IN}$) of 83% is recorded for SSHCI-Only mode, which makes SSHCI technique superior among other low-profile circuits [8], [21], [22] (P_{IN} refers to the measured input power of SSHCI-MPPT chip coming from piezoelectric energy harvester). Compared to the first generation SSHCI presented in [23], both power extraction improvement and efficiency are dropped in this SSHCI-Only mode operation. This originates from power dissipation of newly added voltage reference circuit, energy demanding switching control unit (including switch drivers), and increased switching losses. Maximum measured voltage flipping efficiency (η_F) values are 87.1% and 83.8% for L_{EXT} =100 μH and L_{EXT} =68 μH, respectively. These values change by less than 4% in piezoelectric open circuit voltage $V_{OC,P}$ range between 1.02 V and 3.2 V, while V_{STOR} is fixed at 2.5 V.

Inherent PEH capacitance C_{PZ} plays an important role in the performance characterization of SSHCI interface circuit. As C_{PZ} increases (volume of PEH increases), PEH will convert more mechanical energy into electrical energy, and input power entering interface circuit will rise. Therefore, SSHCI can deliver more output power to the load for increased C_{PZ} values. However, voltage flipping efficiency η_F will drop and relative output power performance improvement over harvested power of an ideal full bridge rectifier (FBR) will be reduced. Still, a low-prolife inductor will be sufficient to operate SSHCI circuit seamlessly while providing reasonable output power levels. This is because compared to other conventional SSHI circuits, voltage flipping occurs in two-step process to invert voltage on C_{PZ}, which restricts the maximum resonating current level [23].

Fig. 23 illustrates measured harvested power levels at optimum storage voltages $V_{STOR,OPT}$ and corresponding Figure-of-Merit (FOM) values of both SSHCI-Only and SSHCI-MPPT operations for different PEH excitation levels (L_{EXT} =100 μH). FOM described previously in [15], [30] indicates how much improvement is obtained over ideal FBR:

$$FOM = \frac{P_{OUT}}{P_{IDEAL-FBR}} = \frac{P_{OUT}}{f_{EX} C_{PZ} V_{OC,P}^2} \tag{12}$$

Main SSHCI operation provides 5.44 maximum FOM while utilizing 100 μH external inductor which occupies 18 mm^3.

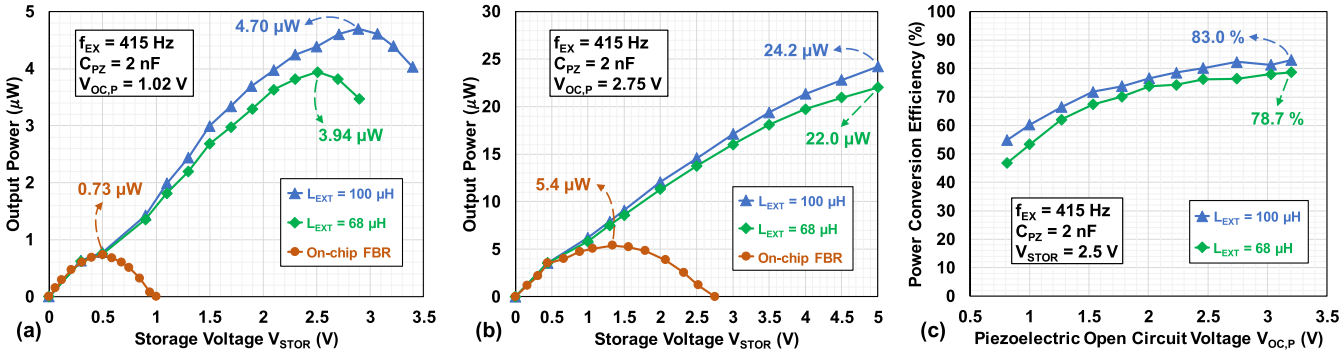

Fig. 22. Measured output power of main SSHCI circuit (SSHCI-Only) for piezoelectric open circuit voltage amplitudes (a) $V_{OC,P} = 1.02$ V, (b) $V_{OC,P} = 2.75$ V, and (c) power conversion efficiency of main SSHCI operation.

TABLE III

COMPARISON OF THE IMPLEMENTED IC WITH STATE-OF-THE-ART

Reference	[14] SECE	[18] SSHI	[19] SSHI	[22] FCR	[8] SE-SSHC	[33] ML-SSHC	[34] AR-MPPT	**This Work (SSHCI)**
Technology	40 nm	350 nm	130 nm	180 nm	180 nm	180 nm	350 nm	**180 nm**
Chip Size	0.55 mm^2	1.17 mm^2	1.07 mm^2	1.70 mm^2	3.90 mm^2	1 mm^2	5.52 mm^2	**1.23 mm^2**
C_{PZ}	43 nF	9 nF	20 nF	80 pF	1.94 nF	6 nF	11 nF	**2 nF**
$V_{OC,P}$	NA	0.95 V	1.6 V	NA	2.5 V	1.27 V	NA	**1.02 V**
f_{EX}	75.4 Hz	229.2 Hz	100 Hz 180 Hz	110 kHz	219 Hz	22 Hz	NA	**415 Hz**
Inductor (Volume)	2.2 mH (0.13 cm^3)	3.3 mH (15.2 cm^3)	3.3 mH (NA)	NO	NO	NO	10 mH (NA)	**68-100 μH (18 mm^3)**
Flipping Time Detection	NA	External Adjustment	External Adjustment	External Adjustment	External Adjustment	NA	NA	**Autonomous Adjustment**
MPPT	NO	YES	YES	NO	NO	NO	YES	**YES**
Cold Start	YES	YES	YES	YES	NO	YES	YES	**YES**
Peak Conversion Efficiency	94%	NA	78[(2)]%	NA	NA	NA	80[(2)]%	**83% (100 μH) 78.7% (68 μH)**
Power Extraction Improvement (FOM[(1)]x100)	314%	440%	417%	483[(3)]%	606[(4)]%	701%	97%	**544% (100 μH) 456% (68 μH)**
Load Sensitivity ($\lvert\Delta P_{OUT}/\Delta V_{OUT}\rvert$)	19.27[(4)] μW/V	2.33[(4)] μW/V	NA	13.97[(4)] μW/V	2.08[(4)] μW/V	NA	NA	**0.88 μW/V ($V_{OC,P}$ = 2.23V) 1.05 μW/V ($V_{OC,P}$ = 1.53V)**

(1) FOM = $P_{STOR}/f_{EX}V_{OC,P}^2C_{PZ}$ (2) It is only for DC/DC converter. (3) Calculated with respect to on-chip FBR. (4) Calculated from paper.

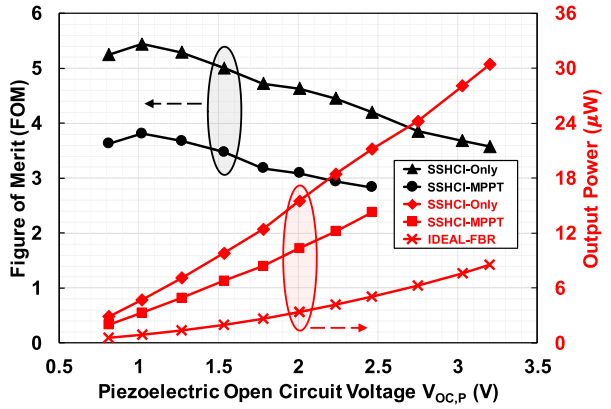

Fig. 23. Measured output power of SSHCI-Only and SSHCI-MPPT modes compared to ideal FBR at different $V_{OC,P}$ levels.

This FOM is the result of weak electromechanical coupling of MEMS PEH, which affects performance of FBR harshly. When MPPT is enabled (SSHCI-MPPT operation), maximum FOM drops to 3.81 due to elevated power consumption coming from MPPT sub-circuits. This power consumption mainly corresponds to switching losses in DC/DC conversion, power dissipation of pulse generators inside MPPT switching control unit and switch drivers. Both SSHCI-Only and SSHCI-MPPT modes perform better at low excitation levels where nonlinear switching technique handles damping force well [30]. Percentage optimum power tracking efficiency waveform of MPPT circuit ($\eta_{P,TRACKING}$) is presented in Fig. 24 along with percentage optimum storage voltage tracking efficiency ($\eta_{V,TRACKING}$) waveform. $\eta_{P,TRACKING}$ and $\eta_{V,TRACKING}$ are calculated using equations below:

$$\eta_{P,TRACKING}(\%) = \frac{P_{SSHCI-MPPT}}{P_{SSHCI-Only,Max}} \times 100, \quad (13)$$

$$\eta_{V,TRACKING}(\%) = \frac{V_{STOR,OPT-MPPT}}{V_{STOR,OPT-Manual}} \times 100. \quad (14)$$

In equation (13), $P_{SSHCI-Only,Max}$ depicts measured maximum output power of SSHCI-Only operation in which supply voltages of all MPPT sub-units are grounded (MPPT is disabled), and $P_{SSHCI-MPPT}$ indicates output power of SSHCI-MPPT operation in which supply voltages of all MPPT sub-units are connected to V_{STOR} (MPPT is enabled). In equation (14), $V_{STOR,OPT-MPPT}$ accounts for optimum storage voltage found by MPPT circuit and $V_{STOR,OPT-Manual}$ expresses

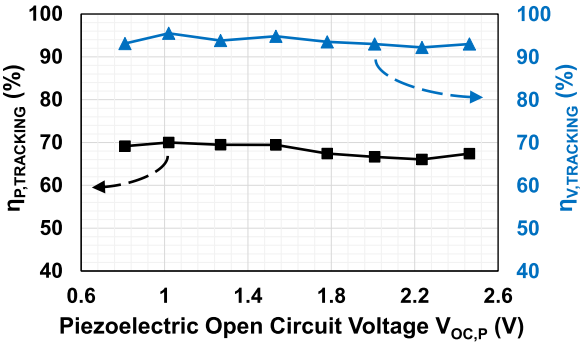

Fig. 24. Measured percentage optimum power tracking efficiency ($\eta_{P,TRACKING}$) and percentage optimum storage voltage tracking efficiency ($\eta_{V,TRACKING}$) waveforms of MPPT circuit at different piezoelectric open circuit voltage amplitudes ($V_{OC,P}$).

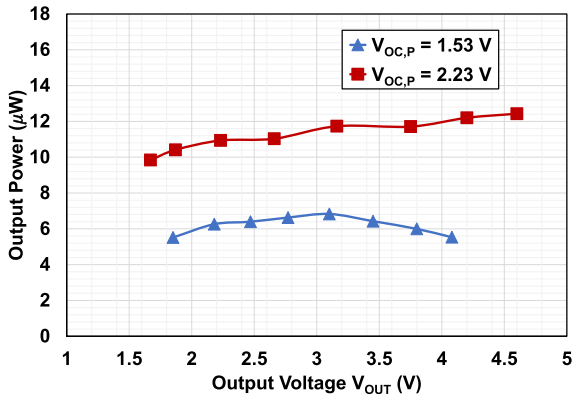

Fig. 25. Measured output power of SSHCI-MPPT circuit vs. V_{OUT} voltage levels for $V_{OC,P} = 1.53$ V and $V_{OC,P} = 2.23$ V ($L_{EXT} = 100\mu$H).

optimum storage voltage found by externally adjusting load resistance R_{LOAD}. MPPT is capable of obtaining $V_{STOR,OPT}$ values with larger than 92% $\eta_{V,TRACKING}$ efficiency. 70% maximum $\eta_{P,TRACKING}$ efficiency is recorded due to power dissipations of MPPT sub-units, DC/DC switching losses, and low input power of the harvesting interface system. The goal of MPPT is not improved FOM, but to achieve better load independence and adaptability to different excitation conditions. Fig. 25 depicts power levels measured at output of MPPT circuit with optimum V_{STOR} voltage levels for two different excitations corresponding to $V_{OC,P}$ =1.53 V and $V_{OC,P}$ =2.23 V. Since MPPT circuit is decoupled from the harvester, dependence of MPPT output on V_{OUT} is low as shown in Fig. 25. Fig. 26 illustrates measured output power versus vibration frequency plot of SSHCI operation at 1 g acceleration. SSHCI circuit is capable of maintaining its operation under different excitation frequencies; however, output power of PEH drops as excitation frequency deviates from the resonance frequency (415 Hz). This leads to lower extracted power levels for vibration frequencies other than PEH resonance frequency.

Table III shows a performance comparison of the validated circuit in this work against state-of-the-art PEH interface circuits. In terms of autonomy, SSHCI circuit distinguishes itself from others, which require external adjustment. Conventional methods may create inconvenience in some biomedical applications demanding fully integrated and autonomous system operation. SECE circuits in [12], [14], [15] suffer

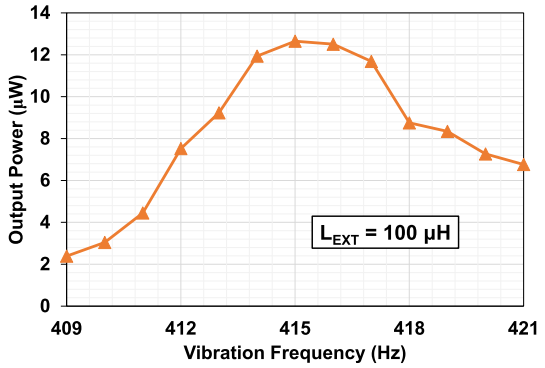

Fig. 26. Measured output power versus vibration frequency plot of SSHCI operation at 1 g acceleration.

from relatively small FOM values. Furthermore, they are more suitable to operate with shock excitations as in [14]. Sanchez *et al.* [18] employed a large external inductor to realize a conventional SSHI interface that can extract energy from both periodic and shock excitations. Although this circuit used an externally controlled MPPT to yield acceptable power levels, it is not suitable for a miniaturized harvesting system.

Recently, Li *et al.* [19] proposed perturb and observe (P&O) method integrated with SSHI circuit that senses output power continually to find optimum. External inductor is shared between SSHI and MPPT blocks as in our system; however, FOM and efficiency fall below the measured values in this work with low-profile components. Inductorless designs in [8], [22], [33] use on-chip capacitors for flipping, which is a positive approach towards miniaturization. They present FOM values better than traditional SSHI circuits. Multilevel SSHC (ML-SSHC) circuit [33] benefits from relatively low excitation frequency of PEH harvester (22 Hz) which shrinks dynamic losses and boosts FOM. Nonetheless, synchronized switch harvesting (SSH) technique is the nature of these inductorless architectures that make them strongly load dependent. Similar to SSHCI-MPPT, Shim and Kim [34] makes use of half open circuit voltage sensing to detect optimum battery voltage. Yet, harvesting circuit relies on an active rectifier (AR) for AC/DC conversion, which leads to small FOM.

SSHCI circuit provides a basis to realize low-profile and autonomous energy harvesting systems owing to its two-step voltage flipping scheme and optimum charge transfer detection. Load sensitivity in Table III is defined as ratio of change in output power with respect to the change in output voltage ($|\Delta P_{OUT}/\Delta V_{OUT}|$). Compared with literature, presented MPPT architecture improves load sensitivity by achieving around 1 μW/V, owing to its dedicated DC/DC conversion operation which decouples C_{OUT} from PEH. MPPT delivers a more robust system solution in exchange for reduction in FOM. SSHCI circuit presented in this work achieves improved power extraction compared to conventional SECE and SSHI methods while using a smaller inductor.

V. Conclusion

A low-cost autonomous piezoelectric energy harvesting interface circuit has been presented in this paper. A small footprint 68-100 μH external inductor has been included in SSHCI

technique to manage voltage flipping via optimum charge flipping detection. A unique MPPT scheme has been proposed to work seamlessly with SSHCI, and boost system robustness while providing load independence. SSHCI-MPPT IC has been implemented in 180 nm CMOS process with 1.23 mm^2 area. The fabricated chip accomplishes a maximum of 5.44x relative performance improvement over ideal FBR, which is greater than conventional nonlinear switching techniques that employ bulky external components. 83% power conversion efficiency has been measured for $V_{OC,P}$ =3.2 V. Proposed harvesting system offers a good alternative to power embedded electronics, and paves the way towards miniaturization.

REFERENCES

[1] H. Ulusan, A. Muhtaroglu, and H. Kulah, "A sub-500 W interface electronics for bionic ears," *IEEE Access*, vol. 7, pp. 132140–132152, 2019.

[2] T. Galchev, J. McCullagh, R. L. Peterson, K. Najafi, and A. Mortazawi, "Energy harvesting of radio frequency and vibration energy to enable wireless sensor monitoring of civil infrastructure," *Proc. SPIE*, vol. 7983, Apr. 2011, Art. no. 798314.

[3] P. D. Mitcheson, E. M. Yeatman, G. K. Rao, A. S. Holmes, and T. C. Green, "Energy harvesting from human and machine motion for wireless electronic devices," *Proc. IEEE*, vol. 96, no. 9, pp. 1457–1486, Sep. 2008.

[4] R. J. M. Vullers, R. Schaijk, H. Visser, J. Penders, and C. Hoof, "Energy harvesting for autonomous wireless sensor networks," *IEEE Solid-State Circuits Mag.*, vol. 2, no. 2, pp. 29–38, Jun. 2010.

[5] F. Dell'Anna *et al.*, "State-of-the-art power management circuits for piezoelectric energy harvesters," *IEEE Circuits Syst. Mag.*, vol. 18, no. 3, pp. 27–48, Aug. 2018.

[6] S. Chamanian, H. Ulusan, A. Koyuncuoğlu, A. Muhtaroğlu, and H. Külah, "An adaptable interface circuit with multi-stage energy extraction for low power piezoelectric energy harvesting MEMS," *IEEE Trans. Power Electron.*, vol. 34, no. 3, pp. 2739–2747, Mar. 2019.

[7] L. Beker, O. Zorlu, N. Goksu, and H. Kulah, "Stimulating auditory nerve with MEMS harvesters for fully implantable and self-powered cochlear implants," in *Proc. 37th 17th Int. Conf. Solid-State Sensors, Actuat. Microsyst., TRANSDUCERS EUROSENSORS*, 2013, pp. 1663–1666.

[8] S. Du, Y. Jia, C. Zhao, G. A. J. Amaratunga, and A. A. Seshia, "A fully integrated split-electrode SSHC rectifier for piezoelectric energy harvesting," *IEEE J. Solid-State Circuits*, vol. 54, no. 6, pp. 1733–1743, Jun. 2019.

[9] T. T. Le, J. Han, A. Von Jouanne, K. Mayaram, and T. S. Fiez, "Piezoelectric micro-power generation interface circuits," *IEEE J. Solid-State Circuits*, vol. 41, no. 6, pp. 1411–1419, May 2006.

[10] Y. Kushino and H. Koizumi, "Piezoelectric energy harvesting circuit using full-wave voltage doubler rectifier and switched inductor," in *Proc. IEEE Energy Convers. Congr. Expo.*, Sep. 2014, pp. 2310–2315.

[11] J. Dicken, P. D. Mitcheson, I. Stoianov, and E. M. Yeatman, "Power-extraction circuits for piezoelectric energy harvesters in miniature and low-power applications," *IEEE Trans. Power Electron.*, vol. 27, no. 11, pp. 4514–4529, Nov. 2012.

[12] M. Dini, A. Romani, M. Filippi, and M. Tartagni, "A nanopower synchronous charge extractor IC for low-voltage piezoelectric energy harvesting with residual charge inversion," *IEEE Trans. Power Electron.*, vol. 31, no. 2, pp. 1263–1274, Feb. 2016.

[13] G. Shi, Y. Xia, X. Wang, L. Qian, Y. Ye, and Q. Li, "An efficient self-powered piezoelectric energy harvesting CMOS interface circuit based on synchronous charge extraction technique," *IEEE Trans. Circuits Syst. I, Reg. Papers*, vol. 65, no. 2, pp. 804–817, Feb. 2018.

[14] A. Morel *et al.*, "A shock-optimized SECE integrated circuit," *IEEE J. Solid-State Circuits*, vol. 53, no. 12, pp. 3420–3433, Dec. 2018.

[15] D. Kwon and G. A. Rincon-Mora, "A single-inductor 0.35 μm CMOS energy-investing piezoelectric harvester," *IEEE J. Solid-State Circuits*, vol. 49, no. 10, pp. 2277–2291, Oct. 2014.

[16] Y. K. Ramadass and A. P. Chandrakasan, "An efficient piezoelectric energy harvesting interface circuit using a bias-flip rectifier and shared inductor," *IEEE J. Solid-State Circuits*, vol. 45, no. 1, pp. 189–204, Jan. 2010.

[17] E. E. Aktakka and K. Najafi, "A micro inertial energy harvesting platform with self-supplied power management circuit for autonomous wireless sensor nodes," *IEEE J. Solid-State Circuits*, vol. 49, no. 9, pp. 2017–2029, Sep. 2014.

[18] D. A. Sanchez, J. Leicht, E. Jodka, E. Fazel, and Y. Manoli, "A 4 μW-to-1 mW parallel-SSHI rectifier for piezoelectric energy harvesting of periodic and shock excitations with inductor sharing, cold start-up and up to 681% power extraction improvement," in *IEEE Int. Solid-State Circuits Conf. (ISSCC) Dig. Tech. Papers*, vol. 59, Feb. 2016, pp. 366–367.

[19] S. Li, A. Roy, and B. H. Calhoun, "A piezoelectric energy-harvesting system with parallel-SSHI rectifier and integrated MPPT achieving 417% energy-extraction improvement and 97% tracking efficiency," in *Proc. Symp. VLSI Circuits*, 2019, pp. 324–325.

[20] L. Wu, X.-D. Do, S.-G. Lee, and D. S. Ha, "A self-powered and optimal SSHI circuit integrated with an active rectifier for piezoelectric energy harvesting," *IEEE Trans. Circuits Syst. I, Reg. Papers*, vol. 64, no. 3, pp. 537–549, Mar. 2017.

[21] S. Du and A. A. Seshia, "An inductorless bias-flip rectifier for piezoelectric energy harvesting," *IEEE J. Solid-State Circuits*, vol. 52, no. 10, pp. 2746–2757, Oct. 2017.

[22] Z. Chen, M.-K. Law, P.-I. Mak, W.-H. Ki, and R. P. Martins, "A 1.7 mm^2 inductorless fully integrated flipping-capacitor rectifier (FCR) for piezoelectric energy harvesting with 483% power-extraction enhancement," in *IEEE Int. Solid-State Circuits Conf. (ISSCC) Dig. Tech. Papers*, Feb. 2017, pp. 372–374.

[23] B. Ciftci *et al.*, "Low-cost fully autonomous piezoelectric energy harvesting interface circuit with up to 6.14x power capacity gain," in *Proc. IEEE Custom Integr. Circuits Conf. (CICC)*, Apr. 2019, pp. 1–4.

[24] T. Hehn *et al.*, "A fully autonomous integrated interface circuit for piezoelectric harvesters," *IEEE J. Solid-State Circuits*, vol. 47, no. 9, pp. 2185–2198, Sep. 2012.

[25] S. Chamanian, B. Ciftci, H. Ulusan, A. Muhtaroglu, and H. Kulah, "Power-efficient hybrid energy harvesting system for harnessing ambient vibrations," *IEEE Trans. Circuits Syst. I, Reg. Papers*, vol. 66, no. 7, pp. 2784–2793, Jul. 2019.

[26] A. Badel *et al.*, "Piezoelectric vibration control by synchronized switching on adaptive voltage sources: Towards wideband semi-active damping," *J. Acoust. Soc. Amer.*, vol. 119, no. 5, pp. 2815–2825, May 2006.

[27] Y. Wu, L. Li, Y. Fan, J. Liu, and Q. Gao, "A linearised analysis for structures with synchronized switch damping," *IEEE Access*, vol. 7, pp. 133668–133685, 2019.

[28] A. Brenes, A. Morel, J. Juillard, E. Lefeuvre, and A. Badel, "Maximum power point of piezoelectric energy harvesters: A review of optimality condition for electrical tuning," *Smart Mater. Struct.*, vol. 29, no. 3, Mar. 2020, Art. no. 033001.

[29] S. Fang *et al.*, "An efficient piezoelectric energy harvesting circuit with series-SSHI rectifier and FNOV-MPPT control technique," *IEEE Trans. Ind. Electron.*, early access, Sep. 10, 2020, doi: 10.1109/TIE.2020.3007054.

[30] S. Chamanian, A. Muhtaroglu, and H. Kulah, "A self-adapting synchronized-switch interface circuit for piezoelectric energy harvesters," *IEEE Trans. Power Electron.*, vol. 35, no. 1, pp. 901–912, Jan. 2020.

[31] L. Costanzo, A. Lo Schiavo, and M. Vitelli, "Power extracted from piezoelectric harvesters driven by non-sinusoidal vibrations," *IEEE Trans. Circuits Syst. I, Reg. Papers*, vol. 66, no. 3, pp. 1291–1303, Mar. 2019.

[32] S. J. Yun, S. S. Kwak, J. Lee, Y. C. Im, S.-G. Lee, and Y. S. Kim, "Asymmetric SECE piezoelectric energy harvester under weak excitation," *IEEE Access*, vol. 8, pp. 99132–99140, 2020.

[33] P. Angelov and M. Nielsen-Lonn, "A fully integrated multi-level synchronized-switch-harvesting-on-capacitors interface for generic PEHs," *IEEE J. Solid-State Circuits*, vol. 55, no. 8, pp. 2118–2128, Aug. 2020.

[34] M. Shim and J. Kim, "Self-powered 30 μW to 10 mW piezoelectric energy harvesting system with 9.09 ms/V maximum power point tracking time," *IEEE J. Solid-State Circuits*, vol. 50, no. 10, pp. 2367–2379, Oct. 2015.